International Journal of Solids and Structures xxx (xxxx) xxx

Contents lists available at ScienceDirect

International Journal of Solids and Structures

journal homepage: www.elsevier.com/locate/ijsolstr

On the effect of plastic anisotropy, strength and work hardening on the tensile ductility of aluminium alloys

Bjørn Håkon Frodal[a,b], David Morin[a,b], Tore Børvik[a,b], Odd Sture Hopperstad[a,b]

[a] Structural Impact Laboratory (SIMLab), Department of Structural Engineering, Norwegian University of Science and Technology (NTNU), NO-7491, Trondheim, Norway
[b] Centre for Advanced Structural Analysis (CASA), NTNU, NO-7491, Trondheim, Norway

ARTICLE INFO

Article history:
Received 3 June 2019
Revised 28 August 2019
Accepted 3 October 2019
Available online xxx

Keywords:
Ductile failure
Strain localization
Anisotropy
Work hardening
Porous plasticity

ABSTRACT

The influence of plastic anisotropy, yield strength and work hardening on ductile failure is studied by nonlinear finite element simulations and strain localization analyses of tensile tests in different material orientations. Three aluminium alloys with different grain structures and crystallographic textures, heat-treated to three conditions giving rise to different yield strength and work-hardening behaviours, are considered. The anisotropic yield surfaces of the alloys, obtained by the crystal plasticity finite element method, are used in the numerical simulations of ductile failure in the tensile tests. In addition, a yield surface for an isotropic material is included for comparison. These yield surfaces are combined with three stress-strain curves representative of the different heat-treatments, resulting in a range of relevant model materials with different plastic anisotropy, yield strength and work hardening used in the numerical investigations. Finite element simulations of tensile tests in seven in-plane directions are carried out, i.e., 0°, 15°, 30°, 45°, 60°, 75° and 90° to the reference direction, and the non-proportional loading histories are used in the subsequent strain localization analyses. Plastic anisotropy is found to have a marked influence on the tensile ductility and to induce failure anisotropy, i.e., a variation in the failure strain with loading direction. The shape and extension of the regions of concentrated plastic flow in the finite element simulations vary with tensile direction for the anisotropic materials. In agreement with previous experimental evidence, the strain localization analyses predict a variation of the failure strain with tensile direction that appears to correlate with the variation of the Lankford coefficient, indicating that the failure anisotropy is closely linked to the plastic anisotropy. The strain localization analyses predict a higher ductility for materials with lower yield strength and higher work hardening, as these features lead to a more distributed plastic deformation and a stress state with a lower stress triaxiality in the neck. This redistribution of the plastic deformation makes the tensile specimen less prone to strain localization and subsequent ductile failure. The influence of yield strength and work hardening is further found to depend on the plastic anisotropy.

1. Introduction

The thermo-mechanical processing of metals influences microstructural characteristics such as the grain structure and the crystallographic texture, and determines the plastic behaviour of these materials. As a result, extruded profiles, rolled plates and other formed structural components typically exhibit plastic anisotropy. The strength of the plastic anisotropy varies, and is mostly governed by the crystallographic texture (Engler and Randle, 2009). Using crystal plasticity theory, which accounts for the crystallographic texture of materials, the yielding and plastic flow of metals are well described (Zhang et al., 2015; 2016). Numerical simulations of materials with crystal plasticity are in general computationally expensive, and phenomenological plasticity models are thus preferred when relatively large structural components are considered. These models may include an anisotropic yield function, typically incorporating one or several linear transformations of the stress tensor (Barlat et al., 2005), which is calibrated from either a large number of experimental tests (Fourmeau et al., 2011) or crystal plasticity simulations (Zhang et al., 2015; 2016; Frodal et al., 2019).

The process of ductile fracture includes nucleation, growth and coalescence of microscopic voids at second-phase particles or inclusions, and depends markedly on the local stress state and

E-mail address: bjorn.h.frodal@ntnu.no (B.H. Frodal).

https://doi.org/10.1016/j.ijsolstr.2019.10.003

Nomenclature

Symbols

$\boldsymbol{\sigma}$	Cauchy stress tensor
$\dot{\lambda}$	Plastic multiplier
$\dot{\mathbf{q}}$	Non-uniformity rate vector
$\dot{p}$	Equivalent plastic strain rate
$\mathbb{C}^t$	Material tangent stiffness tensor
$\mathbf{D}$	Rate-of-deformation tensor
$\mathbf{F}$	Deformation gradient tensor
$\mathbf{I}$	Second-order identity tensor
$\mathbf{L}$	Velocity gradient tensor
$\mathbf{N}$	Nominal stress tensor
$\mathbf{n}$	Unit normal vector to imperfection band
$\mathbf{R}$	Rotation tensor
Φ	Yield function
ϕ, θ	Localization band angles
ϕ_0, θ_0	Initial localization band angles
σ_0	Initial yield stress
σ_t	True stress
σ_{I}, σ_{II}, σ_{III}	Ordered principal stresses
σ_{M}	Matrix flow stress
σ_h	Hydrostatic stress
σ_{vm}	von Mises equivalent stress
ε_f	Macroscopic failure strain
ε_l	Logarithmic strain
φ	Equivalent stress
ξ	Strain rate ratio
A	Cross-section area
a	Yield surface exponent
A_0	Initial cross-section area
D	Cross-section diameter
E, ν	Elastic coefficients
F	Measured force
f	Void volume fraction
f_0	Initial void volume fraction
L	Lode parameter
p	Equivalent plastic strain
p_f	Local equivalent failure strain
Q_i, θ_i	Isotropic hardening parameters
q_i	Tvergaard parameters
S'_k, S''_l	Principal values of transformed stress tensors
T	Stress triaxiality ratio

Abbreviations

ED	Extrusion/reference direction
ND	Normal/thickness direction
TD	Transverse direction

microstructural characteristics in a complex way (Pineau et al., 2016). In turn, the local stress state is governed by the yielding and plastic flow of the material, and it follows that the strength and work hardening of a material can influence the ductility measured in an experimental test. If the material exhibits plastic anisotropy because of the thermo-mechanical processing, the measured ductility could also depend on the direction of loading. For aluminium alloys, experiments show that the tensile ductility decreases with increasing yield stress (Lloyd, 2003; Westermann et al., 2014; Pedersen et al., 2015; Hannard et al., 2016) and is markedly influenced also by plastic anisotropy (Fourmeau et al., 2013; Khadyko et al., 2019). Numerical simulations indicate that this variation in tensile ductility is partially due to differences in the deformation and local stress state within the neck region of the tensile specimen, as a higher yield strength is typically associated with reduced work hardening (Dæhli et al., 2016). A higher stress level

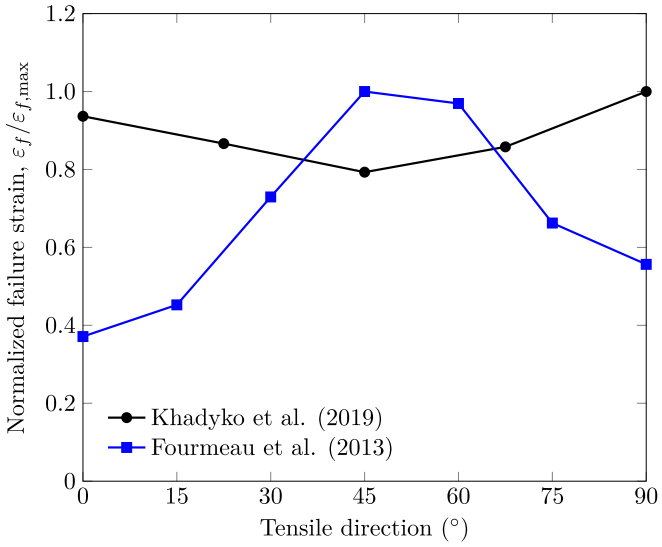

Fig. 1. Normalized failure strain versus tensile direction obtained from tensile tests on a recrystallized AA6063 alloy (Khadyko et al., 2019) and a non-recrystallized AA7075 alloy (Fourmeau et al., 2013) with different crystallographic textures.

may also accelerate void nucleation at second-phase particles or inclusions (Pineau et al., 2016). Ductile failure can also be caused by plastic anisotropy, e.g., triggering shear bands in ductile materials (Benzerga et al., 2019).

There are three main sources of anisotropic failure in metals: *plastic anisotropy*, which primarily stems from the crystallographic texture, *morphological anisotropy*, which originates from the shape and preferred orientation of particles and voids, and *topological anisotropy*, which is a result of the spatial distribution of particles and voids. Albeit, these types of anisotropy originate from the microscale, their effect is usually observed at the macroscale as a variation in the failure strain with loading direction, i.e., failure anisotropy. Experimental evidence from tensile tests on smooth axisymmetric specimens (Fourmeau et al., 2013) and flat rectangular specimens (Khadyko et al., 2019) indicates that the failure anisotropy observed for some aluminium alloys correlates with the plastic flow anisotropy as expressed by the Lankford coefficients. In Fig. 1, failure anisotropy (i.e., that the failure strain varies with tensile direction) is illustrated for a recrystallized AA6063 alloy with recrystallization texture (Khadyko et al., 2019) and a fibrous, non-recrystallized AA7075 alloy with deformation texture (Fourmeau et al., 2013). Whereas the failure anisotropy is significant for both materials, the variation of the failure strain with tensile direction is opposite for the two alloys.

Based on unit cell simulations, Keralavarma et al. (2011) investigated the effects of initial porosity, initial void aspect ratio, stress triaxiality and anisotropy parameters, and showed that the void aspect ratio, in addition to the plastic anisotropy parameters, can significantly affect the overall ductility of anisotropic solids. More recently, Legarth and Tvergaard (2018) performed three-dimensional unit cell simulations investigating the three sources of anisotropic failure. They found that the presence of plastic anisotropy amplifies the predictions obtained for different initial void shapes, and that there was a clear interaction between the effects of plastic anisotropy, void shape and void spacing. Also experimentally the arrangement of second-phase particles has been observed to have an effect on the failure process as well as the failure anisotropy (Hannard et al., 2018). Agarwal et al. (2002) studied the cracking of second-phase particles in an extruded aluminium alloy. They observed that for a given strain level, the number fraction of cracked particles varied depending on the loading direction. Thus void nucleation due to particle cracking can lead to failure anisotropy.

Please cite this article as: B.H. Frodal, D. Morin and T. Børvik et al., On the effect of plastic anisotropy, strength and work hardening on the tensile ductility of aluminium alloys, International Journal of Solids and Structures, https://doi.org/10.1016/j.ijsolstr.2019.10.003

Use of unit cell simulations is an attractive way of studying the mechanisms of ductile failure, as information of the local deformation fields can be employed to get a more profound understanding of the growth and coalescence of voids. In the unit cell modelling framework, ductile failure is usually assumed to correspond to the onset of void coalescence. However, strain localization is often a strong indicator for imminent ductile failure, as plastic deformation and damage evolution localize in a narrow region prior to failure initiation. Based on unit cell simulations, Tekoğlu et al. (2015) showed that depending on the stress triaxiality, strain localization occurs simultaneously or prior to void coalescence. Thus, the strain localization phenomenon can be considered as an indicator for incipient ductile failure.

The imperfection band approach to localization analysis, first proposed by Marciniak and Kuczyński (1967) for plane stress states, and later extended by Rice (1976) to a general and rigorous formulation, can be applied to study and predict the initiation of ductile failure. A material with an imperfection is considered where the properties are slightly different inside the imperfection compared to the rest of the material. When the material is subjected to loading, deformation tends to concentrate inside the imperfection and this tendency promotes localization of deformation in the material. The imperfection is taken in the form of a planar band, and the stress and strain fields inside and outside of the band are homogeneous but different. Localization by loss of ellipticity occurs when the strain rate becomes infinite inside the imperfection band. To trigger loss of ellipticity, the imperfection band must incorporate a softening mechanism (Rudnicki and Rice, 1975) in the case of associated plastic flow, and this is usually achieved by use of a porous plasticity model describing the constitutive behaviour inside the band. The material outside the band is described either by metal plasticity or porous plasticity. The imperfection band approach has recently been used in several studies, and good quantitative agreement is observed both with unit cell simulations (Morin et al., 2018a; Morin et al., 2019; Reddi et al., 2019; Vishwakarma and Keralavarma, 2019) and experimental tests (Gruben et al., 2017; Morin et al., 2018b; 2019). Whereas several studies have used unit cell simulations to investigate void growth and coalescence in anisotropic materials (Keralavarma et al., 2011; Dæhli et al., 2017a; Legarth and Tvergaard, 2018; Frodal et al., 2019), localization analyses with finite element-based unit cells have so far only been performed for isotropic materials (Barsoum and Faleskog, 2007; Barsoum and Faleskog, 2011; Dunand and Mohr, 2014; Dæhli et al., 2017b; Guo and Wong, 2018; Vishwakarma and Keralavarma, 2019). Using these computationally expensive finite element models to perform strain localization analyses for anisotropic solids is still difficult even with modern computers. A large number of localization band orientations has to be investigated within a three-dimensional setup for each load case and results in prohibitive computational times.

In this study, the influence of plastic anisotropy, strength and work hardening on the initiation of ductile failure in tension is investigated numerically with the use of the strain localization theory. Thus, incipient ductile failure will in the following be considered to occur at the instance when strain localization is first encountered in the material. Experimental data from tension tests on three extruded aluminium alloys obtained in previous studies (Khadyko et al., 2014; Frodal et al., 2019) is used as backdrop for the numerical study. These alloys have different grain structures and crystallographic textures, and were solution heat-treated and artificially aged to three conditions giving different strength and work-hardening behaviour. The anisotropic yield surfaces of the alloys were obtained by crystal plasticity simulations. Based on these experimental results, a set of fictitious, but relevant, aluminium materials are designed that exhibit different combinations of strength, work hardening and plastic anisotropy. Finite element simulations of tensile tests on smooth axisymmetric specimens are performed for each of these materials in seven in-plane directions, i.e., 0°, 15°, 30°, 45°, 60°, 75° and 90° to the reference direction. Subsequently, the non-proportional loading histories from the finite element simulations are used in strain localization analyses to predict incipient ductile failure of the tensile specimens, and thus to investigate the effect of plastic anisotropy, strength and work hardening on the tensile ductility. It is important to investigate these effects together in order to disclose any interaction effects on the tensile ductility. In order to incorporate the plastic anisotropy of the materials, the porous plasticity model proposed by Dæhli et al. (2017a), incorporating the anisotropic yield criterion Yld2004-18p (Barlat et al., 2005), is applied in all simulations.

2. Experimental background

The tensile ductility of the aluminium alloys AA6060, AA6082.25 and AA6082.50 has been examined experimentally in previous studies (Khadyko et al., 2014; Frodal et al., 2019). These alloys were provided by Hydro Aluminium as extruded rectangular profiles, with a thickness of 10 mm and a width of 83 mm, from which axisymmetric tensile specimens were machined. The specimens were solution heat-treated and artificially aged to three different tempers, namely temper O (annealed), temper T7 (overaged) and temper T6 (peak strength).

The three aluminium alloys have different grain structures and crystallographic textures (Frodal et al., 2017) leading to different plastic anisotropy (Frodal et al., 2019). The AA6060 alloy has

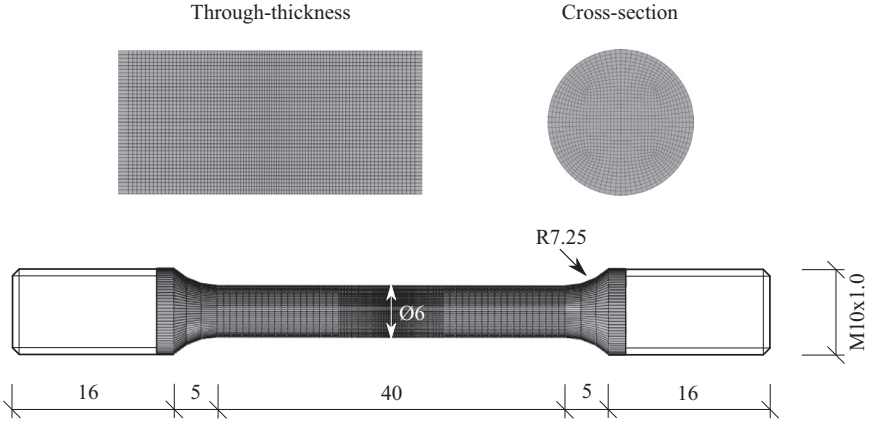

Fig. 2. Axisymmetric tensile specimen with the finite element mesh. The through-thickness and cross-section mesh is shown from the centre of the specimen. Dimensions are in mm.

Please cite this article as: B.H. Frodal, D. Morin and T. Børvik et al., On the effect of plastic anisotropy, strength and work hardening on the tensile ductility of aluminium alloys, International Journal of Solids and Structures, https://doi.org/10.1016/j.ijsolstr.2019.10.003

a recrystallized grain structure comprising equi-axed grains, and exhibits a cube texture with a minor Goss component. A typical fibrous, non-recrystallized grain structure is observed for the AA6082.25 alloy, which has a cube texture with orientations along the β-fibre. The AA6082.50 alloy has recrystallized grain structure with large elongated grains and a rotated cube texture (Frodal et al., 2017). For further details about the materials, the reader is referred to Khadyko et al. (2014) and Frodal et al. (2017, 2019), and for further information on the texture components in FCC materials, see, e.g., Engler and Randle (2009).

Axisymmetric tensile specimens, see Fig. 2, were used to determine the work-hardening response and ductile failure properties of the materials (Khadyko et al., 2014; Frodal et al., 2019). All of the specimens were oriented along the transverse direction (TD) of the extruded profile. A displacement-controlled test machine with a constant cross-head velocity of 1.2 mm/min was used to perform the tests. During testing, the force and diameters along the extrusion direction (ED) and thickness direction (ND) of the minimum cross-section of the specimen were continuously measured until fracture using a load cell and an in-house laser-based measuring system (Frodal et al., 2017), respectively.

The current area of the specimen can be estimated by

$$A = \frac{\pi}{4} D_1 D_3 \tag{1}$$

where D_1 and D_3 are the measured diameters in ED and ND, respectively. The true stress over the minimum cross-section area is

$$\sigma_t = \frac{F}{A} \tag{2}$$

where F is the measured force. Assuming plastic incompressibility and negligible elastic strains, the logarithmic (or true) strain is given by

$$\varepsilon_l = \ln\left(\frac{A_0}{A}\right) \tag{3}$$

where A_0 is the initial cross-section area of the specimen, and σ_t and ε_l represent average values over the minimum cross-section area of the specimen.

Fig. 3 presents the true stress-strain curves from the tensile tests in TD plotted up to the point of failure, where marked differences between the behaviour of the different alloy and temper combinations can be observed. Note that failure is here defined as the point of maximum true stress, and an abrupt decrease in the stress level is observed after this point. The strength and work hardening of the different tempers of the same alloy are distinct. In general, the O tempers have the highest work hardening, but the lowest strength. The T6 tempers have the lowest work hardening and the highest strength, while the T7 tempers are between the O and T6 tempers when it comes to strength and work hardening, see also Section 3.2. Comparing the alloys, the strength clearly varies between them, and also the work hardening is different. Typically, the strength of the two AA6082 alloys for the same temper is similar and higher than that of the AA6060 alloy. The only exception is for the O temper, where the AA6082.25 alloy has higher strength than the two other alloys. The reason for this is primarily that for the two AA6082 alloys in tempers T6 and T7 the precipitate number densities are higher than for the lean AA6060 alloy, whereas for the O temper the main contributions to the yield strength come from elements in solid solution, the dispersoid number density and the grain structure (sub-grain structure).

Comparing the point of failure for the various alloy-temper combinations, makes it apparent that the AA6060 alloy is by far the most ductile alloy and the O temper is the most ductile temper for each alloy. Even the least ductile temper of the AA6060 alloy, i.e, the T6 temper, has a much higher failure strain than all of the tempers of the two AA6082 alloys. Comparing the two AA6082 alloys, it is observed that the AA6082.25 alloy has, in general, a higher failure strain than the AA6082.50 alloy, for the same temper. The lower ductility observed for the AA6082.50 alloy can be linked to the grain structure of this alloy, see Section 5.

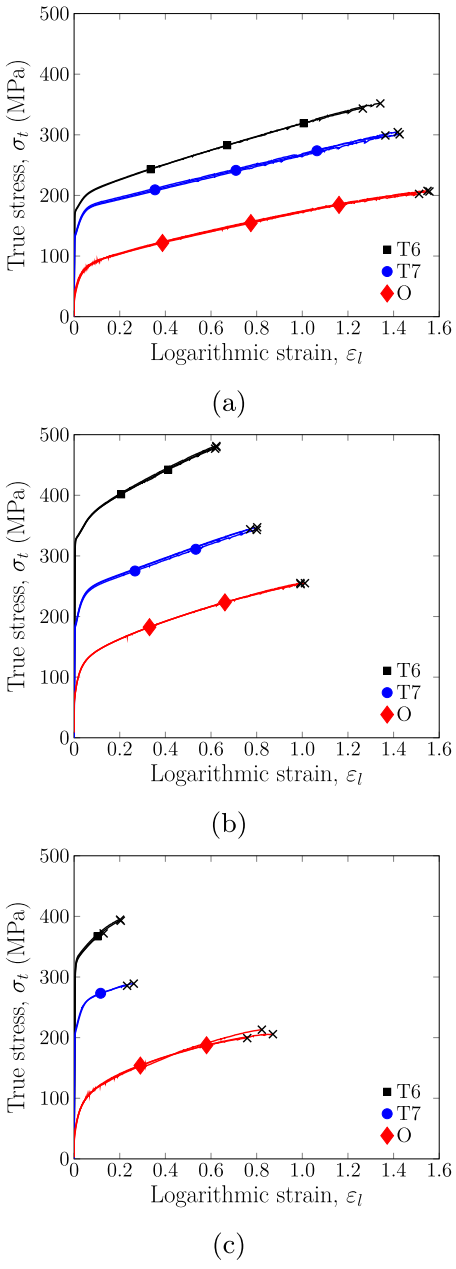

Fig. 3. True stress-strain curves from tension tests of the aluminium alloys (a) AA6060, (b) AA6082.25, and (c) AA6082.50 in tempers T6, T7 and O. All tests were performed with tensile direction along TD of the extruded profile. The data is taken from Khadyko et al. (2014) and Frodal et al. (2017, 2019).

Fig. 4 shows the average failure strain from the tensile tests in TD versus the initial yield stress at 0.2% plastic strain. It is clearly visible that the magnitude of the failure strain, and thus the ductility of the materials, vary with yield strength, and also the difference in ductility between the alloys is evident. In previous studies on various aluminium alloys, it has been found that the failure strain tends to decrease linearly with increasing yield strength for similar microstructure (Lloyd, 2003; Westermann et al., 2014; Pedersen et al., 2015; Hannard et al., 2016), and the reader is referred to these studies for detailed discussions on the physical interpreta-

Please cite this article as: B.H. Frodal, D. Morin and T. Børvik et al., On the effect of plastic anisotropy, strength and work hardening on the tensile ductility of aluminium alloys, International Journal of Solids and Structures, https://doi.org/10.1016/j.ijsolstr.2019.10.003

- Continuing equilibrium:
$$\mathbf{n}\cdot\dot{\mathbf{N}}_b = \mathbf{n}\cdot\dot{\mathbf{N}}_o \quad (4)$$
- Constitutive equations outside the band:
$$\dot{\mathbf{N}}_o = \mathbb{C}_o^t : \mathbf{L}_o \quad (5)$$
- Constitutive equations inside the band:
$$\dot{\mathbf{N}}_b = \mathbb{C}_b^t : \mathbf{L}_b \quad (6)$$
- Equation system for the non-uniformity rate vector $\dot{\mathbf{q}}$:
$$\left(\mathbf{n}\cdot\mathbb{C}_b^t\cdot\mathbf{n}\right)\cdot\dot{\mathbf{q}} = \mathbf{n}\cdot\left(\mathbb{C}_o^t - \mathbb{C}_b^t\right) : \mathbf{L}_o \quad (7)$$

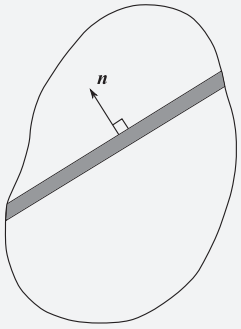

- Compatibility:
$$\mathbf{L}_b = \mathbf{L}_o + \dot{\mathbf{q}}\otimes\mathbf{n} \quad (8)$$
- Band orientation in updated configuration:
$$\mathbf{n} = \begin{bmatrix}\cos\phi\\ \cos\theta\sin\phi\\ \sin\theta\sin\phi\end{bmatrix} \quad (9)$$
- Localization conditions:
$$\det\left(\mathbf{n}\cdot\mathbb{C}_b^t\cdot\mathbf{n}\right) = 0 \quad (10)$$
$$\xi = \sqrt{\frac{\mathbf{D}_b : \mathbf{D}_b}{\mathbf{D}_o : \mathbf{D}_o}} \to \infty \quad (11)$$

Box 1. Overview of the strain localization analyses (Morin et al., 2018a)[1].

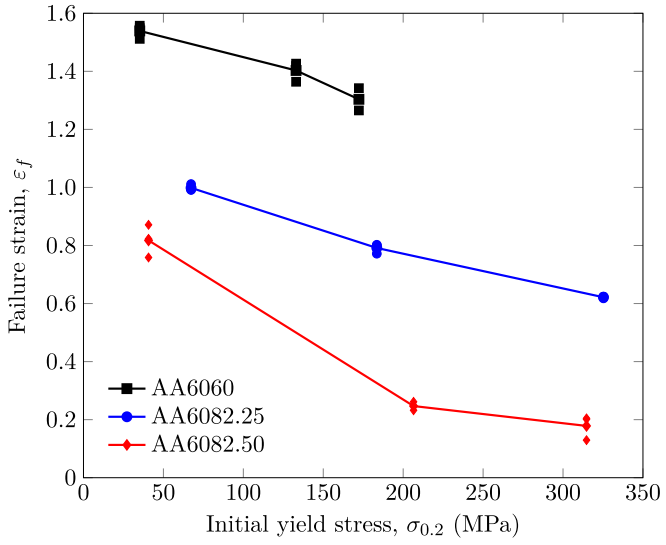

Fig. 4. Failure strain in tension versus initial yield stress at 0.2% plastic strain for the three alloys in different tempers.

tion of these experimental trends. In short, the yield strength of a material is closely linked to its work hardening, and typically as the strength increases, the work hardening decreases, which is negative for the ductility, see Section 4. A higher stress level may also accelerate void nucleation at second-phase particles (Pineau et al., 2016).

3. Numerical methods

3.1. Strain localization theory

The strain localization theory is used herein to investigate the influence of strength, work hardening and plastic anisotropy on the tensile failure of ductile materials. At moderate stress triaxialities, localization has been found to occur simultaneously as void coalescence (Tekoğlu et al., 2015). This is true under a random distribution of voids (Reddi et al., 2019; Vishwakarma and Keralavarma, 2019), and strain localization can thus be useful in predicting incipient ductile failure. As already mentioned, we will define incipient ductile failure as the instance when strain localization is first encountered in the material, and the location of failure initiation is within the finite element where strain localization occurs first, i.e., a critical element, see Section 3.3.

The imperfection band approach proposed by Rice (1976) is used in this study. This method considers a material consisting of two homogeneous regions, which are separated by a thin planar imperfection band, and subjected to an overall uniform deformation. The constitutive equations inside and outside of the imperfection band are allowed to be different, with the requirement that equilibrium and compatibility conditions are enforced across the band. A brief overview of the governing equations of the imperfection band approach is given in Box 1. The reader is referred to Rice (1976), Needleman and Rice (1978), and Morin et al. (2018a,b) for further details.

While this method does not impose any restrictions on the constitutive equations of the material inside or outside the imperfection band, the same approach as in Nahshon and Hutchinson (2008), Gruben et al. (2017), and Morin et al. (2018a, 2018b, 2019) is used in the current work. A porous plasticity model is used to represent the material inside and outside of the imperfection band. It is assumed that any damage mechanism occurring outside of the band is negligible and that the porosity here is zero ($f = 0$), whereas inside the band an imperfection is introduced by pre-existing voids ($f_0 > 0$). For moderate stress triaxialities, encountered in physical tension tests, this is usually an appropriate assumption (Xue et al., 2010; 2013; Westermann et al., 2014). Note that also other types of imperfections can be included both inside and outside the band, e.g., void nucleation (Morin et al., 2018a; 2018b; 2019) and void softening in shear (Nahshon and Hutchinson, 2008; Morin et al., 2018a) can be introduced in the constitutive equations.

An overview of the porous plasticity model used herein is given in Box 2. The heuristic modification of the Gurson (1977) model proposed by Dæhli et al. (2017a) and applied by Morin et al. (2018b) is used in the current study. This extension introduces the equivalent stress of the Yld2004-18p yield function (Barlat et al., 2005) into the constitutive equations, in order to include anisotropic yielding and plastic flow. For zero porosity, the yield criterion reduces to the original Yld2004-18p yield function (Barlat et al., 2005). The porous plasticity model introduces material softening inside the imperfection band, which triggers loss of ellipticity of the governing equations, i.e., strain localization. When an associated flow rule is adopted, material softening is required for loss of ellipticity to occur (Rudnicki and Rice, 1975) and thus for the localization conditions (Box 1) to be met for reasonable stress levels. Note that the Gurson-Tvergaard yield function (Gurson, 1977; Tvergaard, 1981), Equation (15), is derived using von Mises plasticity,

[1] Note that in Morin et al. (2019), there is a typo in Equations (26) and (27). The correct expressions are here given in Equations (5) and (6) of Box 1.

Please cite this article as: B.H. Frodal, D. Morin and T. Børvik et al., On the effect of plastic anisotropy, strength and work hardening on the tensile ductility of aluminium alloys, International Journal of Solids and Structures, https://doi.org/10.1016/j.ijsolstr.2019.10.003

- Corotational formulation:

$$\hat{\boldsymbol{\sigma}} = \mathbf{R}^T \cdot \boldsymbol{\sigma} \cdot \mathbf{R} \quad \wedge \quad \hat{\mathbf{D}} = \mathbf{R}^T \cdot \mathbf{D} \cdot \mathbf{R} \tag{12}$$

- Additive decomposition of strain rate:

$$\hat{\mathbf{D}} = \hat{\mathbf{D}}^e + \hat{\mathbf{D}}^p \tag{13}$$

- Generalized Hooke's law on rate form:

$$\dot{\hat{\boldsymbol{\sigma}}} = \frac{E}{1+\nu}\hat{\mathbf{D}}'^e + \frac{E}{3(1-2\nu)}\mathrm{tr}\left(\hat{\mathbf{D}}^e\right)\mathbf{I} \tag{14}$$

- Yield function:

$$\Phi = \left(\frac{\varphi(\hat{\boldsymbol{\sigma}})}{\sigma_{\mathrm{M}}}\right)^2 + 2q_1 f \cosh\left(\frac{q_2 \mathrm{tr}(\hat{\boldsymbol{\sigma}})}{2\sigma_{\mathrm{M}}}\right) - 1 - q_3 f^2 \leq 0 \tag{15}$$

- Equivalent stress:

$$\varphi\left(\hat{\boldsymbol{\sigma}}\right) = \left(\frac{1}{4}\sum_{k=1}^{3}\sum_{l=1}^{3}\left|S'_k - S''_l\right|^a\right)^{\frac{1}{a}} \tag{16}$$

- Isotropic work hardening:

$$\sigma_{\mathrm{M}} = \sigma_0 + \sum_{i=1}^{3} Q_i\left(1 - \exp\left(-\frac{\theta_i}{Q_i}p\right)\right) \tag{17}$$

- Associated flow rule:

$$\hat{\mathbf{D}}^p = \dot{\lambda}\frac{\partial\Phi}{\partial\hat{\boldsymbol{\sigma}}} \tag{18}$$

- Equivalent plastic strain:

$$p = \int_0^t \dot{p}\, d\bar{t} = \int_0^t \frac{\hat{\boldsymbol{\sigma}} : \hat{\mathbf{D}}^p}{(1-f)\,\sigma_{\mathrm{M}}}\, d\bar{t} \tag{19}$$

- Evolution of void volume fraction:

$$\dot{f} = (1-f)\,\mathrm{tr}\left(\hat{\mathbf{D}}^p\right) \tag{20}$$

- Kuhn-Tucker conditions:

$$\Phi \leq 0, \quad \dot{\lambda} \geq 0, \quad \dot{\lambda}\Phi = 0 \tag{21}$$

Box 2. Overview of the porous plasticity model (Dæhli et al., 2017a).

and the only modification introduced here is that the macroscopic von Mises equivalent stress is replaced by Equation (16). Also other porous anisotropic plasticity models have been developed by, e.g, Benzerga and Besson (2001), and Steglich et al. (2010). The porous plasticity model used here has been validated against unit cell simulations by Dæhli et al. (2017a), and for further details regarding the accuracy of such heuristically extended models, the reader is referred to Dæhli et al. (2017a, 2019).

The strain localization theory by the imperfection band approach has been implemented in a stand-alone Fortran programme, as described in detail by Morin et al. (2018a). The porous plasticity model has been implemented into a user material subroutine (UMAT) for Abaqus/Standard (Abaqus, 2014).

3.2. Finite element analyses

The imperfection band analyses are driven by loading histories extracted from finite element analyses of tensile tests. The axisymmetric tensile specimen is modelled in Abaqus/Standard, and the finite element mesh is presented in Fig. 2. Linear eight-node solid elements with selective reduced integration (C3D8) are used. The dimensions of the elements located in the centre of the specimen are $0.10 \times 0.15 \times 0.15$ mm^3, with the shortest element length along the tensile direction.

The material behaviour of the tensile specimen is defined by the porous plasticity model described in Box 2. When running the finite element simulations of the tensile tests, the initial porosity is set to zero ($f_0 = 0$), thus reducing the model to the anisotropic Yld2004-18p plasticity model (Barlat et al., 2005) with isochoric plastic flow. The effect of porosity in the finite element simulations is thus neglected as f will be zero throughout these simulations. Isotropic elasticity is assumed with a Young's modulus of $E = 70000$ MPa and a Poisson's ratio of $\nu = 0.3$, which are relevant values for aluminium alloys.

In order to study the effect of plastic anisotropy on the tensile ductility, typical yield surfaces for textured aluminium alloys are employed in the simulations. The AA6060 and AA6082.25 alloys have typical recrystallization and deformation texture, respectively, whereas the AA6082.50 alloy has a typical texture of an alloy with large recrystallized grains, see Section 2. In addition, the yield surface of an isotropic alloy with random texture is included for comparison. To emphasise that the yield surfaces from these alloys in the following will be combined with flow stress curves that do not belong to the respective alloy, we will consider the alloys as model materials and rename them accordingly. The model materials are thus denoted alloy A, B, C and D with yield surface belonging to alloy AA6060, AA6082.25 AA6082.50 and an isotropic material, respectively. The yield surfaces of the model materials are presented in Fig. 5 depicted in the ED-TD plane. It is apparent that the yield surfaces for the alloys are distinct due to the crystallographic texture. These anisotropic yield surfaces have previously been found by Frodal et al. (2019) using crystal plasticity finite element analyses. The yield surface of the isotropic material (alloy D) is given by the Yld2004-18p yield function with all anisotropy coefficients equal to one, thus reducing it to an isotropic high-exponent yield function. The exponents of the selected anisotropic yield surfaces are approximately 12. Thus, to limit the influence of the yield surface curvature on the imperfection band analyses, as studied by Dæhli et al. (2017b), the exponent of the isotropic material is set to $a = 12$. The list of anisotropy parameters is omitted in this paper, and the reader is referred to Frodal et al. (2019) for further details.

Fig. 6 presents the normalized yield stresses and Lankford coefficients as function of the tensile direction in the ED-TD plane obtained with the selected yield surfaces. The Lankford coefficient is defined as

$$R_\alpha = \frac{d\varepsilon_\perp}{d\varepsilon_{\mathrm{ND}}} \tag{22}$$

where $d\varepsilon_\perp$ is the incremental strain in the direction perpendicular to the loading direction lying in the ED-TD plane and $d\varepsilon_{\mathrm{ND}}$ is the incremental strain in the thickness direction (ND). Thus, the Lankford coefficient R_α gives the evolution of the cross-section of the specimen. The 0° direction is along ED, and is taken as the reference direction in this study, while the 90° direction is along TD of the extruded profile. Both the values and the variation of the normalized yield stresses and Lankford coefficients are markedly different for the anisotropic yield surfaces. The two curves appear to exhibit the opposite trend for a given anisotropic yield surface, i.e., when the normalized yield stress has a maximum/minimum, the Lankford coefficient tends to have a minimum/maximum. These extrema are caused by the crystallographic texture of the alloys.

In order to study the influence of strength and work hardening on ductile failure, selected work-hardening curves typical for aluminium alloys will be used. The selected work-hardening behaviour is taken from the AA6082.25 alloy artificially aged to the three conditions given in Section 2. The work-hardening rule de-

Please cite this article as: B.H. Frodal, D. Morin and T. Børvik et al., On the effect of plastic anisotropy, strength and work hardening on the tensile ductility of aluminium alloys, International Journal of Solids and Structures, https://doi.org/10.1016/j.ijsolstr.2019.10.003

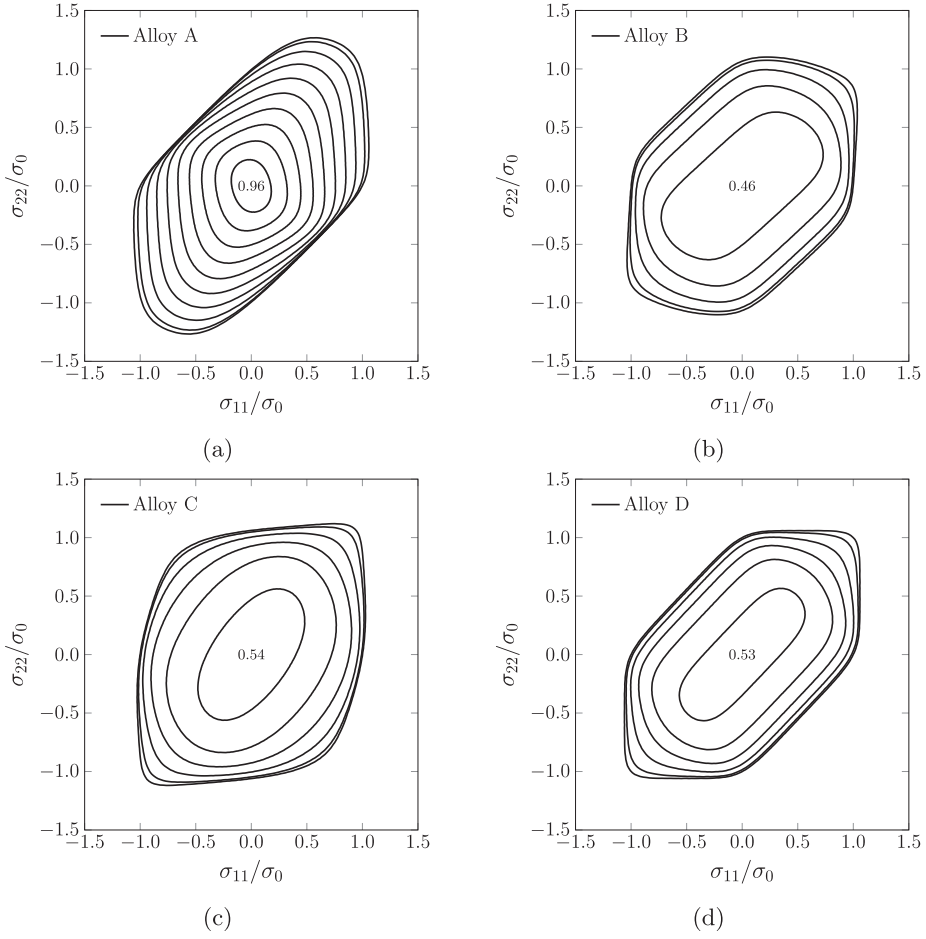

Fig. 5. Yield surfaces depicted in the ED-TD plane for (a) alloy A (AA6060), (b) alloy B (AA6082.25), (c) alloy C (AA6082.50), and (d) alloy D (isotropic). Contours of increasing normalized shear stress are plotted in 0.1 increments, with the maximum value in the centre.

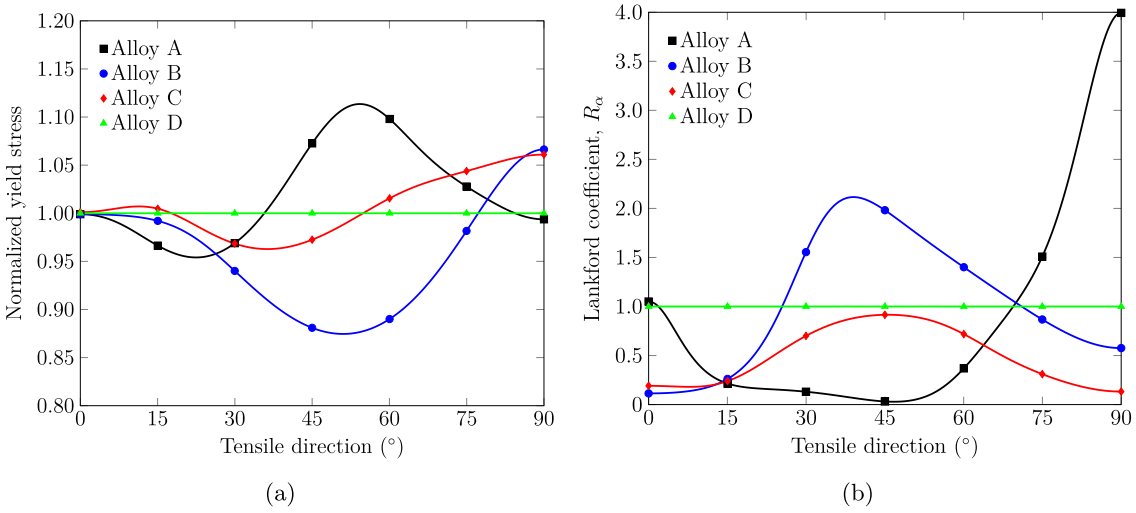

Fig. 6. (a) Normalized yield stress and (b) Lankford coefficient versus tensile direction for uniaxial tension in the ED-TD plane obtained with the four selected yield surfaces.

fined in Box 2 was calibrated in Frodal et al. (2019) using an optimization procedure. Fig. 7 presents the normalized flow stress curves and displays the large difference in work hardening between the three tempers. The corresponding initial yield stress and work-hardening parameters are given in Table 1.

In the following, the simulation procedure consists of finite element analyses of the tensile tests in seven in-plane directions, i.e., 0°, 15°, 30°, 45°, 60°, 75° and 90° with respect to the reference direction (ED). Strain localization theory will be used to predict the logarithmic failure strain in each simulation of a tensile test, see Section 3.3. Note that only initiation of failure is predicted by using the strain localization theory in the post-processing of the finite element simulation results.

Please cite this article as: B.H. Frodal, D. Morin and T. Børvik et al., On the effect of plastic anisotropy, strength and work hardening on the tensile ductility of aluminium alloys, International Journal of Solids and Structures, https://doi.org/10.1016/j.ijsolstr.2019.10.003

Table 1
Initial yield stress and work-hardening parameters (Frodal et al., 2019).

Temper	σ_0 (MPa)	θ_1 (MPa)	Q_1 (MPa)	θ_2 (MPa)	Q_2 (MPa)	θ_3 (MPa)	Q_3 (MPa)
O	57.6	2661.3	44.6	382.2	32.6	120.8	91.0
T7	163.6	1300.1	28.9	1301.2	40.7	52.3	232.9
T6	299.5	470.5	28.5	485.0	29.8	50.0	279.4

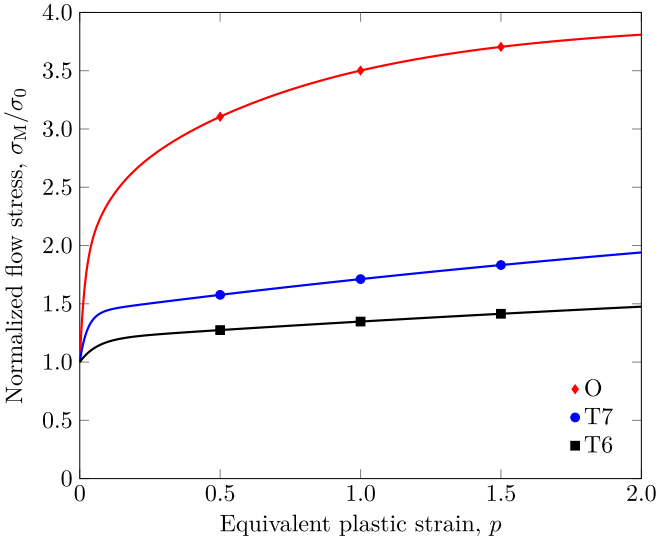

Fig. 7. Normalized flow stress curves representing the work-hardening behaviours used in the numerical study.

3.3. Localization analyses

When performing the imperfection band analyses, the material inside the imperfection band is described by the porous plasticity model in Box 2 with an initial porosity of $f_0 = 0.005$, while outside, the porosity is set to zero as in the finite element simulations. This value of f_0 gives failure strains using the localization analyses that are reasonable for aluminium alloys, and is chosen for all the materials in order to isolate the effects of strength, work hardening and plastic anisotropy on the failure strain. The porous plasticity parameters by Tvergaard (1981) are here given standard values of $q_1 = 1.5$, $q_2 = 1.0$ and $q_3 = q_1^2$, but could alternatively be calibrated for each combination of yield surface and flow stress curve, as done by Dæhli et al. (2017a).

The location of ductile failure initiation is not known a priori, but it is reasonable to assume that failure is first encountered within the neck of the tensile specimen. Accordingly, all elements within this region are examined for strain localization using the imperfection band approach as described in Box 1. The numerical procedure is as follows (Morin et al., 2018b):

1. The deformation gradient $\mathbf{F}(t)$ of each element within the neck region is calculated based on the nodal displacements and the isoparametric shape functions.
2. An imperfection analysis is run for each of these elements based on the extracted deformation gradient $\mathbf{F}(t)$ for a large number of band orientations (approximately 700 unique band orientations for each element) defined by $\phi_0 \in [0,\ \pi]$ and $\theta_0 \in [0,\ 2\pi]$, using a domain reduction method as described in Morin et al. (2018a).
3. For each element, a local failure strain p_f is calculated as the minimum over all imperfection band orientations of the equivalent plastic strain outside the imperfection band at loss of ellipticity inside the band.
4. Using the relationship between the local equivalent plastic strain p of the elements and the macroscopic logarithmic strain ε_l from the finite element simulation of the specimen, the macroscopic failure strain ε_f corresponding to strain localization within the actual element is found.
5. The actual logarithmic failure strain corresponds to the minimum value of ε_f over the neck region and its position is assumed to be the location of failure initiation.

For further details on the numerical procedure the reader is referred to Morin et al. (2018b, 2019). In the subsequent sections, the localization band will refer to the band for which loss of ellipticity occurs first in the critical element, thus the imperfection band giving the lowest macroscopic failure strain ε_f.

4. Numerical results

4.1. Macroscopic behaviour

Fig. 8 presents the true stress-strain curves from the finite element analyses of the tensile tests along the reference direction (ED). All of the materials represented by the yield surfaces in Fig. 5 are shown with the three work-hardening behaviours, and are plotted until failure predicted by the imperfection band approach. It is evident that both the plastic anisotropy, and the strength and work hardening have a pronounced effect on the failure strain, whereas the stress-strain curves are almost identical between the different yield surfaces in the reference direction. In the other tensile directions, variations are observed as the yield stress varies with tensile direction according to the plastic anisotropy defined by the yield surface, see Fig. 6a. Note that, al-

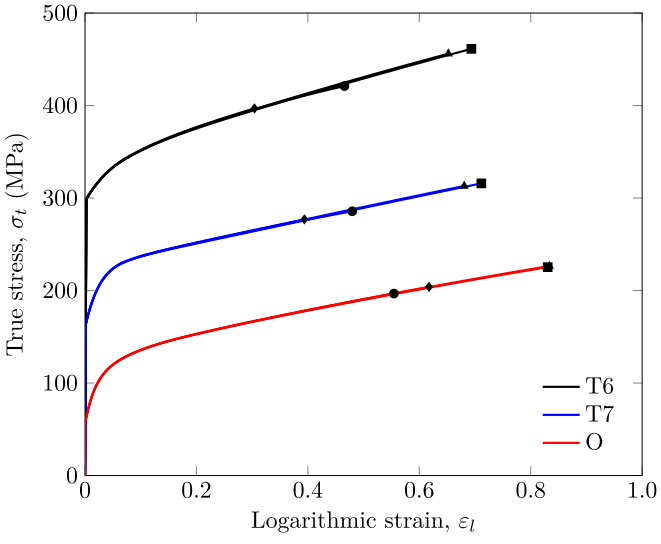

Fig. 8. True stress-strain curves from the finite element analyses of the tensile tests along the reference direction (ED), where the curves are plotted until failure as predicted by the strain localization theory for each material. The location of predicted failure, is shown with the corresponding symbols used in Fig. 9: (■) alloy A, (●) alloy B, (✦) alloy C, (▲) alloy D. The uppermost curve is for temper T6, the intermediate for temper T7 and the lower for temper O.

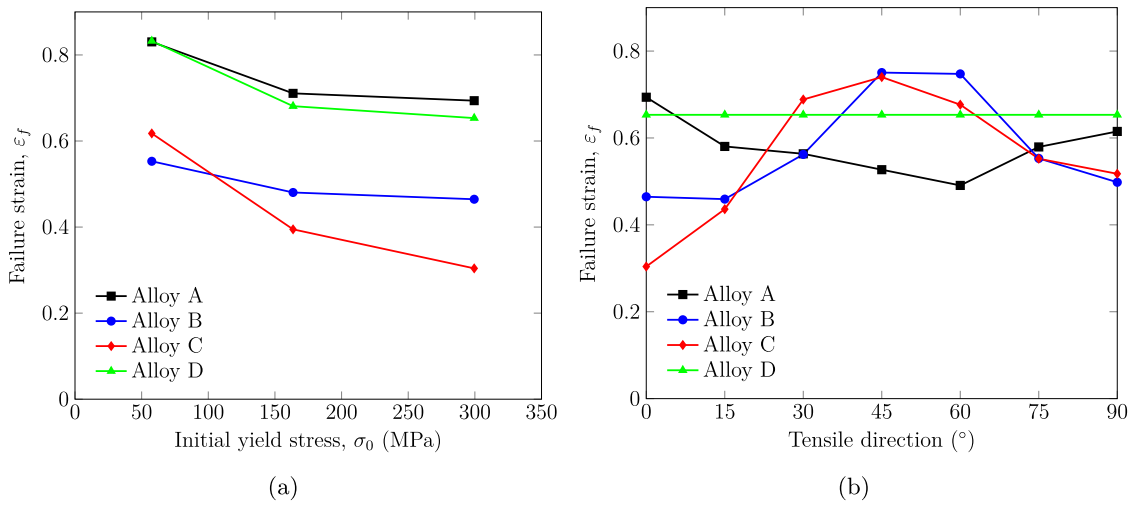

Fig. 9. (a) Failure strain versus initial yield stress for loading along the reference direction (ED), and (b) failure strain versus tensile direction in the ED-TD plane for the alloys with the temper T6 work hardening.

though the macroscopic stress-strain curves are indistinguishable in the reference direction, the local stress state varies with the plastic anisotropy, see Section 4.2.

In Fig. 9a, the predicted failure strain is plotted against the initial yield stress for all materials. The effect of strength and work hardening is seen to vary with the plastic anisotropy. For the lowest strength and highest work hardening (temper O), alloys A and D have approximately the same failure strain, which is significantly higher than the failure strains of alloys B and C. In this temper, alloy B has somewhat lower ductility than alloy C. For higher strength and lower work hardening (tempers T6 and T7), however, alloys B and C switch position, and the failure strain becomes clearly lower for alloy C than for alloy B. The difference in ductility between alloys A and D remains small in tempers T6 and T7, but alloy A has somewhat higher ductility than alloy D. Thus, the decrease in failure strain with increasing strength and decreasing work hardening depends markedly upon the plastic anisotropy.

Fig. 9b presents the failure strain versus the tensile direction in the ED-TD plane for the alloys with the temper T6 work hardening, i.e., the highest strength and lowest work hardening. The failure strain of the anisotropic materials varies significantly with the tensile direction, while for the isotropic alloy (alloy D) the failure strain is constant. The failure strain, and thus the tensile ductility of alloy A, is the greatest in ED (0° direction), whereas alloys B and C have the highest ductility when loaded in the 45° direction. The lowest failure strain is observed in the 60°, 15° and 0° directions for alloys A, B, and C, respectively. Comparing the variation of the failure strain in Fig. 9b with the variation of the Lankford coefficient in Fig. 6b, it is found that these two characteristics exhibit to some extent the same trends, and exhibit an approximately inverse correlation with the normalized yield stress in Fig. 6a, see Section 4.2 for further details. The predicted variation of the failure strain with tensile direction also resembles experimental observations from the literature reproduced in Fig. 1. The predictions for alloy A exhibit the same trend as the experimental data for the AA6063 alloy in Khadyko et al. (2019), and the experimental findings in Fourmeau et al. (2013) for a AA7075 alloy are similar to the predictions for alloy B. These alloys have similar grain structure and crystallographic texture to those presented in Fig. 1.

Plots of the deformed configuration of the tensile specimen at failure predicted by the imperfection band analyses are shown in Fig. 10, as obtained in the finite element simulations of the tensile tests in different directions with respect to the reference direction (ED). Regions of concentrated plastic flow is observed in the centre of the specimen. The shape of these regions is defined by the plastic anisotropy as described by the yield surface and the associated flow rule. Between the materials, different deformation modes are seen, and the level of equivalent plastic strain at failure varies between the materials and with the tensile direction. For the tests along ED and TD, the region of concentrated plastic flow is symmetric about the material axes due to the orthotropic sample symmetry, whereas in the other directions the region of concentrated plastic flow develops at an angle to the loading axis. A reasonable conjuncture is that these deformation modes lead to different shapes of fractured specimens, varying between cup-and-cone to slant shear fracture modes due to the anisotropic plastic flow. However, with the current approach, based on a posteriori localization analyses, only incipient ductile failure can be described. The deformed shapes obtained here for alloy B are similar to the fracture modes observed experimentally by Fourmeau et al. (2013). In addition to plastic anisotropy, material inhomogeneities, e.g., the arrangement of second-phase particles, can contribute to the ductile failure process and affect the fracture path (Hannard et al., 2018). Failure initiation, as predicted by the strain localization theory, is observed to occur in the region of the highest equivalent plastic strain, and for alloys B, C and D, failure initiates in the centre for all loading directions. For alloy A, failure initiates in the centre for all loading directions with the 45° direction as an exception. In this loading direction, failure initiation occurs further towards the specimen periphery. Note that the imperfection band of the strain localization analyses should not be confused with the regions of concentrated plastic flow within the neck of the tensile specimens in the finite element simulations.

Fig. 11 depicts contour plots of the equivalent plastic strain on the minimum cross-section of the tensile tests in the 0° and 90° directions for alloy B in temper T6. The equivalent plastic strain is observed to be more concentrated in the centre of the specimen in the 0° direction, which is linked to the very low value of the Lankford coefficient in this direction, see Fig. 6b. In the 90° direction, the Lankford coefficient is markedly higher and this contributes to a more uniform plastic strain distribution across the specimen's cross-section, which is positive for the tensile ductility. As a result, alloy B has a slightly higher failure strain in the 90° direction than in the 0° direction, see Fig. 9b, even though the stress level is higher in the 90° direction, see Fig. 6a. The effect of plastic flow

Please cite this article as: B.H. Frodal, D. Morin and T. Børvik et al., On the effect of plastic anisotropy, strength and work hardening on the tensile ductility of aluminium alloys, International Journal of Solids and Structures, https://doi.org/10.1016/j.ijsolstr.2019.10.003

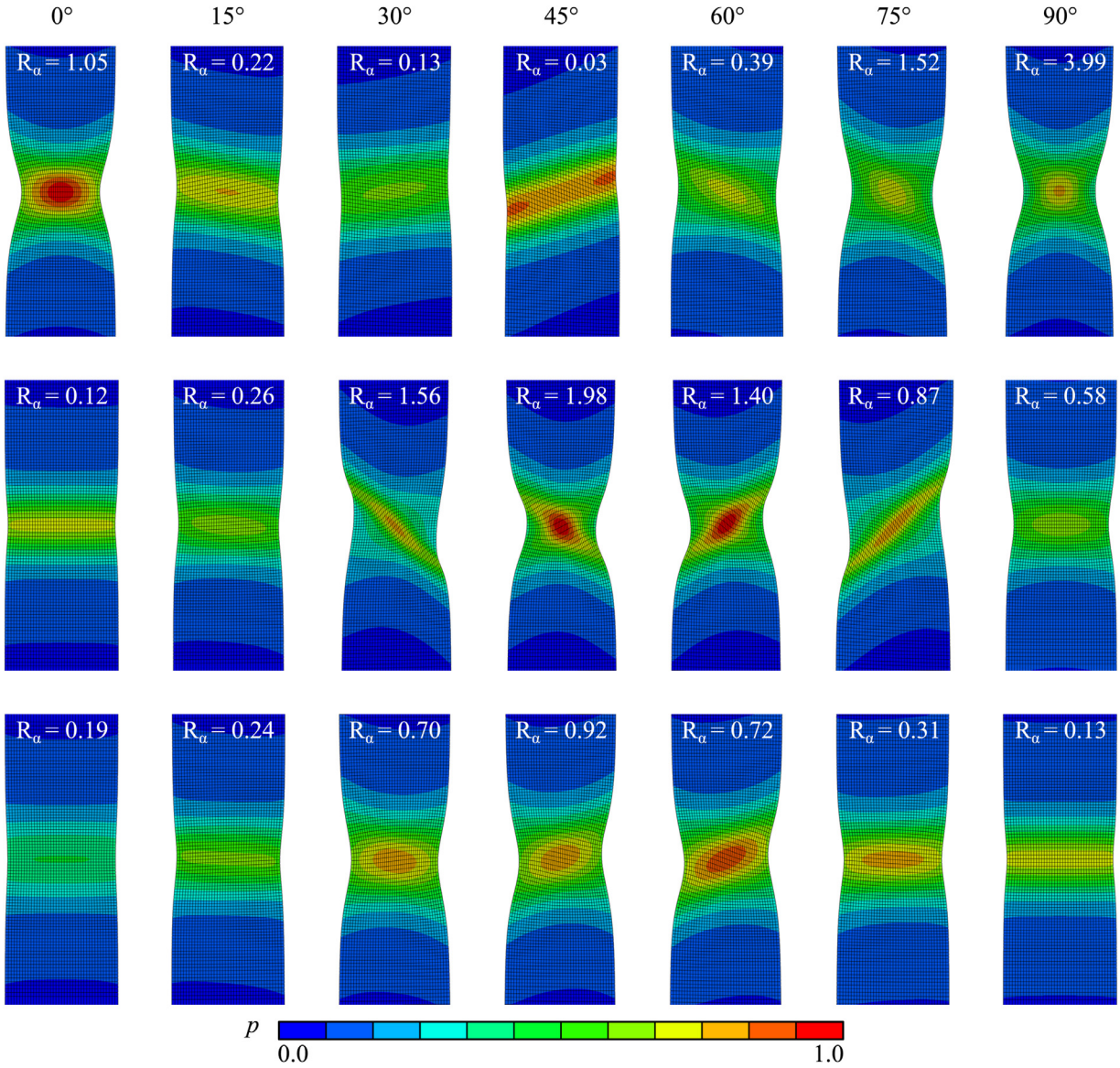

Fig. 10. Deformed configuration of the tensile specimen at failure (as predicted by the imperfection band analysis) depicted in the ED-TD plane as obtained from the simulations of tensile tests in different directions with respect to the reference direction (ED): (top) alloy A, (middle) alloy B, and (bottom) alloy C, with work hardening according to temper T6. Contours of the equivalent plastic strain are shown on the deformed meshes. The Lankford coefficient R_α of the corresponding test is depicted on the top of each mesh.

on ductility will be further discussed in the next section—and particularly in connection with Fig. 14.

4.2. Microscopic behaviour

In this section, we look more closely into the microscopic behaviour of the critical element in the neck region of the tensile specimen, i.e., the location of failure initiation. Relevant quantities both inside and outside of the imperfection band from the strain localization analyses are investigated in order to further interpret the effects of strength, work hardening and plastic anisotropy on strain localization. It is therefore useful to define certain stress invariants, such as the stress triaxiality ratio and Lode parameter to be used in the following. The stress triaxiality ratio is defined as

$$T = \frac{\sigma_h}{\sigma_{vm}} \tag{23}$$

where $\sigma_h = \frac{1}{3}\mathrm{tr}(\boldsymbol{\sigma})$ is the hydrostatic stress and $\sigma_{vm} = \sqrt{\frac{3}{2}\boldsymbol{\sigma}' : \boldsymbol{\sigma}'}$ is the von Mises equivalent stress, $\boldsymbol{\sigma}'$ being the stress deviator. The Lode parameter is defined as

$$L = \frac{2\sigma_{\mathrm{II}} - \sigma_{\mathrm{I}} - \sigma_{\mathrm{III}}}{\sigma_{\mathrm{I}} - \sigma_{\mathrm{III}}} \tag{24}$$

where $\sigma_{\mathrm{I}} \geq \sigma_{\mathrm{II}} \geq \sigma_{\mathrm{III}}$ are the ordered principal stresses. Note that the Lode parameter is $L = -1$ for generalized axisymmetric tension, $L = 0$ for generalized shear, and $L = +1$ for generalized axisymmetric compression.

Fig. 12 presents quantities from the imperfection band analyses obtained inside and outside of the critical imperfection band in the critical element from the simulations of the tensile tests in the reference direction (ED) for alloys A, B, C and D in temper T6. The normalized von Mises stress, inside and outside the band, together with the normalized void volume fraction inside the band, are plotted against the logarithmic strain in Fig. 12a. The von Mises

Please cite this article as: B.H. Frodal, D. Morin and T. Børvik et al., On the effect of plastic anisotropy, strength and work hardening on the tensile ductility of aluminium alloys, International Journal of Solids and Structures, https://doi.org/10.1016/j.ijsolstr.2019.10.003

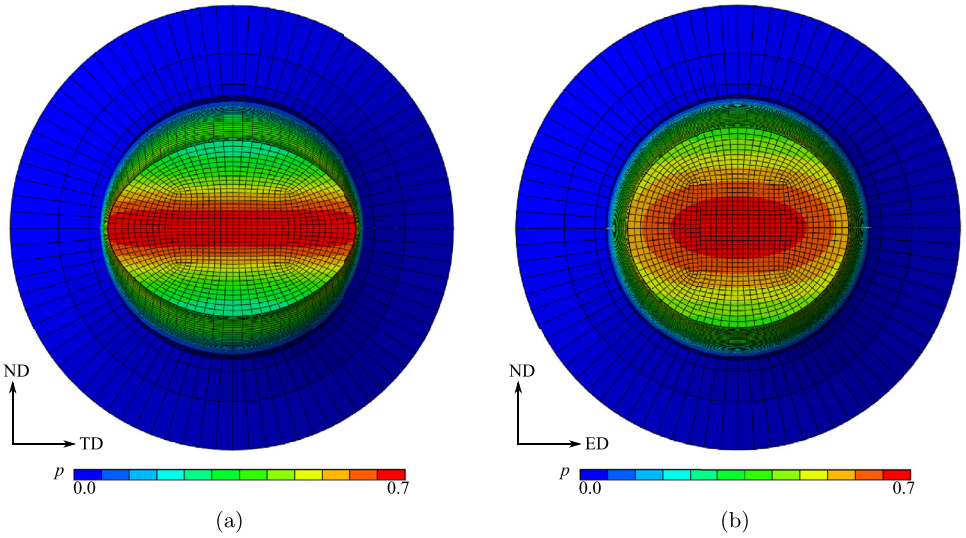

Fig. 11. Minimum cross-section at failure (as predicted by the imperfection band analysis) of alloy B with the temper T6 work hardening showing contours of the equivalent plastic strain for simulations of tensile tests in the: (a) 0° direction, and (b) 90° direction.

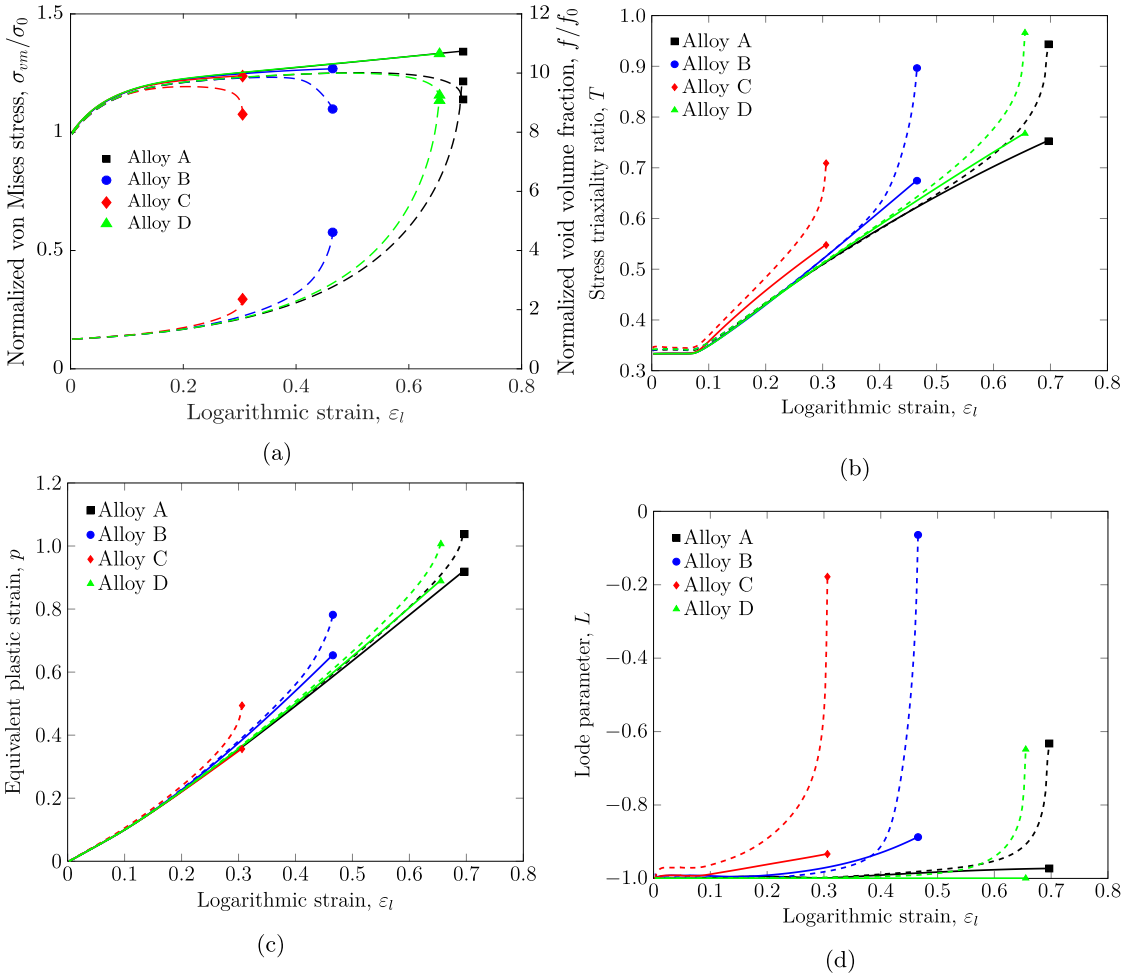

Fig. 12. Local behaviour in the regions inside (dashed lines) and outside (solid lines) of the imperfection band in the critical element for the materials with work hardening according to temper T6 loaded along ED: (a) normalized von Mises stress and normalized void volume fraction, (b) stress triaxiality ratio, (c) equivalent plastic strain, and (d) Lode parameter versus logarithmic strain over the neck.

Please cite this article as: B.H. Frodal, D. Morin and T. Børvik et al., On the effect of plastic anisotropy, strength and work hardening on the tensile ductility of aluminium alloys, International Journal of Solids and Structures, https://doi.org/10.1016/j.ijsolstr.2019.10.003

stress is similar outside of the band for all alloys, whereas inside the band the material experiences porosity induced softening before localization occurs. Initially, the evolution of the porosity is similar for all materials, but with straining the porosity inside the band grows differently depending on the material and thus the plastic anisotropy. As shown in Fig. 9, alloys A and C have respectively the highest and lowest failure strain for this configuration. Softening is seen to occur earlier for alloy C than for the other alloys, owing to the rapid increase of the porosity at a lower value of the logarithmic strain in the neck. The stress triaxiality is plotted against the logarithmic strain in Fig. 12b. After necking, the stress triaxiality increases with straining, but with a higher rate inside the imperfection band than outside, and strain softening inside the band coincides with a rapid increase of the stress triaxiality. Compared with the other alloys, alloy C has higher stress triaxiality both outside and inside the imperfection band for all strains, which explains the lower ductility. An earlier rapid increase of the stress triaxiality inside the band is seen for the alloys with the lowest ductility, namely alloys B and C. The equivalent plastic strain p inside and outside of the critical imperfection band is plotted in Fig. 12c as a function of the logarithmic strain ε_l over the neck. Outside of the imperfection band, the equivalent plastic strain evolves similarly for all alloys, whereas inside the evolution differs. The material inside the band experiences a higher equivalent plastic strain rate than outside to compensate for the porosity-induced softening, which occurs at different strain levels for the four materials. Fig. 12d displays the Lode parameter L inside and outside of the imperfection band as a function of the logarithmic strain ε_l over the neck. It is apparent that the stress state drifts from generalized tension ($L = -1$) towards generalized shear ($L = 0$) inside the imperfection band, as also observed by Morin et al. (2018a,b). The stress state is also observed to differ slightly from generalized tension outside of the imperfection band due to the plastic anisotropy. For the materials with the lowest ductility, e.g., alloy C, the stress state inside of the band is observed to change rapidly from generalized tension towards generalized shear at a lower logarithmic strain than for the more ductile materials, e.g., alloy A.

In Fig. 13 the same quantities as in Fig. 12 are shown, but here the simulations of the tension tests in the reference direction (ED) for alloy A in tempers O, T7 and T6 are addressed. The trends seen in Fig. 13 are representative for the other alloys as well. The porosity is seen to grow the fastest for the T6 temper and the slowest for the O temper, i.e., a higher work hardening leads to a lower growth rate of the porosity as a function of the logarithmic strain over the neck of the tensile specimen, see Fig. 13a. In the simulations for the O temper, the stress triaxiality increases with a clearly lower rate than for the other two tempers with higher strength and lower work hardening, see Fig. 13b. Thus, for a given logarithmic strain after necking, the stress triaxiality is definitely the lowest for the O temper, which is partly the reason for the higher tensile ductility. The stress triaxiality ratio is found to be higher close to strain localization for the T6 temper than for the T7 temper, both inside and outside of the imperfection band. From Fig. 13c it is evident that the lower strength and higher work hardening of the O temper lead to a more gradual increase in the equivalent plastic strain as the logarithmic strain over the neck increases compared with the T6 and T7 tempers. The higher work hardening contributes to a more uniform plastic strain distribution throughout the cross-section of the tensile specimen, which delays the formation of a neck and thus strain localization. Albeit not as apparent, the equivalent plastic strain inside and outside of the imperfection band evolves faster for the T6 temper than for the T7 temper. As seen in Fig. 13d, the stress state appears to drift earlier from generalized tension towards generalized shear for tempers T6 and T7 than for temper O due to the higher strength and lower work hardening. It seems as if the plastic anisotropy might have a stronger impact on the stress state within the neck region for a material with lower work hardening. A lower work-hardening rate gives a sharper and faster evolving neck region which will affect the stress state in the neck so that it drifts earlier from its original state of uniaxial tension.

Fig. 14 presents the microscopic behaviour of alloy B in temper T6 from simulations of the tension tests in the 0°, 45°, and 90° directions. In agreement with Fig. 6a, the von Mises stress level is clearly different in the three directions, see Fig. 14a. The evolution of the porosity is also different in the three directions, where the void growth is the slowest in the 45° direction, which has the lowest von Mises stress. Initially, the void growth is lower in the 0° direction than in the 90° direction, but this changes in the final stage before localization. From Fig. 14b, it can be observed that the stress triaxiality level inside the imperfection band at a given logarithmic strain over the neck is higher in the 0° direction with the lowest ductility. Outside the imperfection band, the 90° direction has a slightly lower stress triaxiality level than the 45° direction, and the 0° direction is also here the direction with the highest stress triaxiality level.

In the 45° direction, the equivalent plastic strain rate is lower than in the other directions, see Fig. 14c. This indicates that the plastic deformation is more dispersed over the specimen's cross-section, which is favourable to prevent strain localization. Again, the stress state is seen to drift from generalized tension ($L = -1$) towards generalized shear ($L = 0$) inside of the imperfection band, and the drift occurs first in the 0° direction exhibiting the lowest ductility. Due to the plastic anisotropy defined by the yield surface and the associated plastic flow rule, the Lode parameter is seen to evolve differently for different tensile directions also outside the imperfection band.

5. Discussion

The failure predictions presented in Fig. 9 obtained in the strain localization analyses are found to capture the trends observed experimentally. In agreement with the experimental data in Fig. 4, the localization analyses in Fig. 9a give a lower failure strain for a material with a higher strength and lower work hardening. Also, the failure strain is observed to vary with plastic anisotropy and the influence of strength and work hardening is different depending on the alloy. Albeit good agreement is achieved between the numerical and experimental trends, there are certain mechanisms not included in the numerical study that can have a substantial effect on the failure strain. For instance, in the experiments for the AA6060 and AA6082.25 alloys, the difference in the failure strain between the O and T7 tempers and the T7 and T6 tempers is similar, but numerically a smaller difference is observed between the T7 and T6 tempers. A reasonable explanation for this finding is that the stress level for the T6 temper is sufficiently high to make void nucleation a more important mechanism for damage evolution (Pineau et al., 2016), which is not captured by the porous plasticity model used herein, considering only growth of pre-existing voids. For the AA6082.50 alloy, a large decrease in the failure strain between the O and T7 tempers is observed experimentally. This finding and the lower overall ductility observed for the AA6082.50 alloy can be linked to the grain structure, as the large grains of this alloy increase the amount of intercrystalline fracture and reduce the tensile ductility (Frodal et al., 2017).

Although plastic anisotropy related to the crystallographic texture can lead to variations in the failure strain both between alloys and with tensile direction as seen in the numerical study, other sources of anisotropy can influence the ductile failure process and affect the failure anisotropy. Even materials exhibiting nearly isotropic yielding and plastic flow can exhibit failure anisotropy

Please cite this article as: B.H. Frodal, D. Morin and T. Børvik et al., On the effect of plastic anisotropy, strength and work hardening on the tensile ductility of aluminium alloys, International Journal of Solids and Structures, https://doi.org/10.1016/j.ijsolstr.2019.10.003

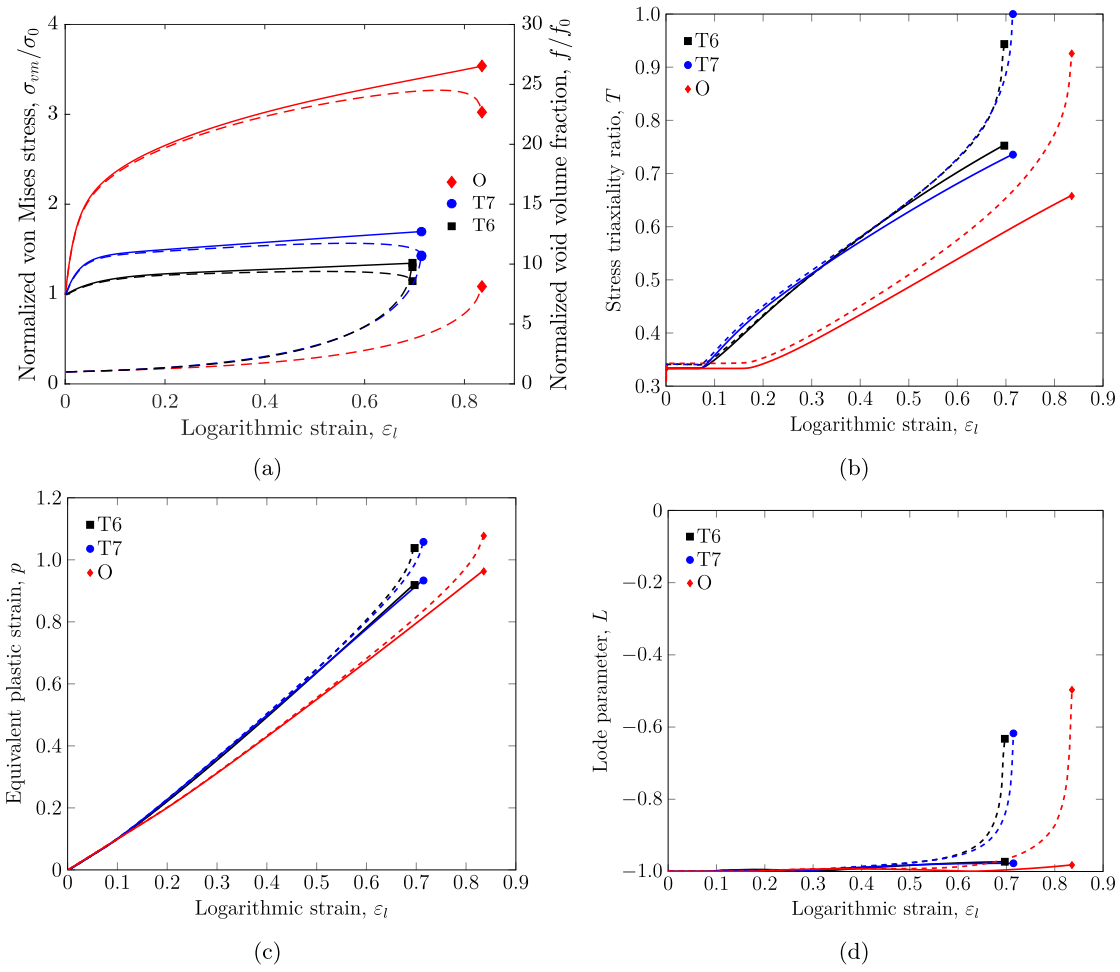

Fig. 13. Local behaviour in the regions inside (dashed lines) and outside (solid lines) of the imperfection band in the critical element for alloy A with the three different flow stress curves loaded along ED: (a) normalized von Mises stress and normalized void volume fraction, (b) stress triaxiality ratio, (c) equivalent plastic strain, and (d) Lode parameter versus logarithmic strain over the neck.

because of morphological or topological anisotropy caused by the shape, orientation and spatial distribution of voids and particles (Hannard et al., 2018). As investigated by Agarwal et al. (2002), the loading direction can affect the particle cracking process, as the number fraction of cracked particles can depend on the direction of loading. Thus, void nucleation by particle cracking can introduce anisotropic effects. Also the spatial distribution of particles and clusters can influence the void coalescence process and lead to failure anisotropy (Hannard et al., 2018). It has also been shown by unit cell analyses that the void aspect ratio can significantly affect the overall ductility (Keralavarma et al., 2011) and that plastic anisotropy can amplify this effect (Legarth and Tvergaard, 2018).

It was quite apparent from Fig. 10 that the plastic anisotropy has an influence on the deformation mode at incipient ductile failure of the specimen, as the shape and extension of the regions of concentrated plastic flow vary with tensile direction for the anisotropic materials. It is a reasonable conjuncture that the variation in shape of the regions can change the failure mode from cup-and-cone failure to slant shear failure depending on the plastic anisotropy and loading direction. These failure modes are typically observed experimentally for anisotropic materials (Chen et al., 2011; Fourmeau et al., 2013). This was also recently studied by Benzerga et al. (2019), who showed that anisotropic plasticity can effectively trigger shear bands and cause failure of ductile materials.

From the strain localization analyses, it was evident that the stress states in the regions inside and outside of the imperfection band in the critical element depend on the plastic anisotropy of alloys A, B, and C, see Fig. 12. The stress state inside of the imperfection band was seen to be strongly affected by the plastic anisotropy, and that this has a great influence on the failure strain predicted by the strain localization theory. Higher work-hardening rate is favourable for delaying failure as it delays necking and distributes the plastic deformation over a wider area of the specimen's cross-section. This will in turn affect the local stress state inside the specimen so that, e.g., the stress triaxiality is reduced for a given value of the logarithmic strain over the neck, cf. Fig. 13.

The failure strain varies with tensile direction for anisotropic materials and the plastic anisotropy of alloy B was found to affect the stress state both inside and outside of the imperfection band, see Fig. 14. A lower stress level was observed to give an increase in the ductility, but also the value of the Lankford coefficient affects the ductility, since it governs the distribution of the plastic deformation across the specimen cross-section. A Lankford coefficient close to unity will distribute the plastic deformations more uniformly and thus be positive for the ductility, cf. Fig. 11. Albeit a lower stress level, caused by the anisotropy in yield stress, appears to increase the ductility, the effect of the stress triaxiality and Lode parameter seems to be even greater. As an example, in the simulations of the tensile tests of alloy B, the stress level is lower in the 0° direction than in the 90° direction, but even so the ductility is lower in the former direction. The reason for the lower ductility in the 0° direction is that the stress triaxiality and the Lode pa-

Please cite this article as: B.H. Frodal, D. Morin and T. Børvik et al., On the effect of plastic anisotropy, strength and work hardening on the tensile ductility of aluminium alloys, International Journal of Solids and Structures, https://doi.org/10.1016/j.ijsolstr.2019.10.003

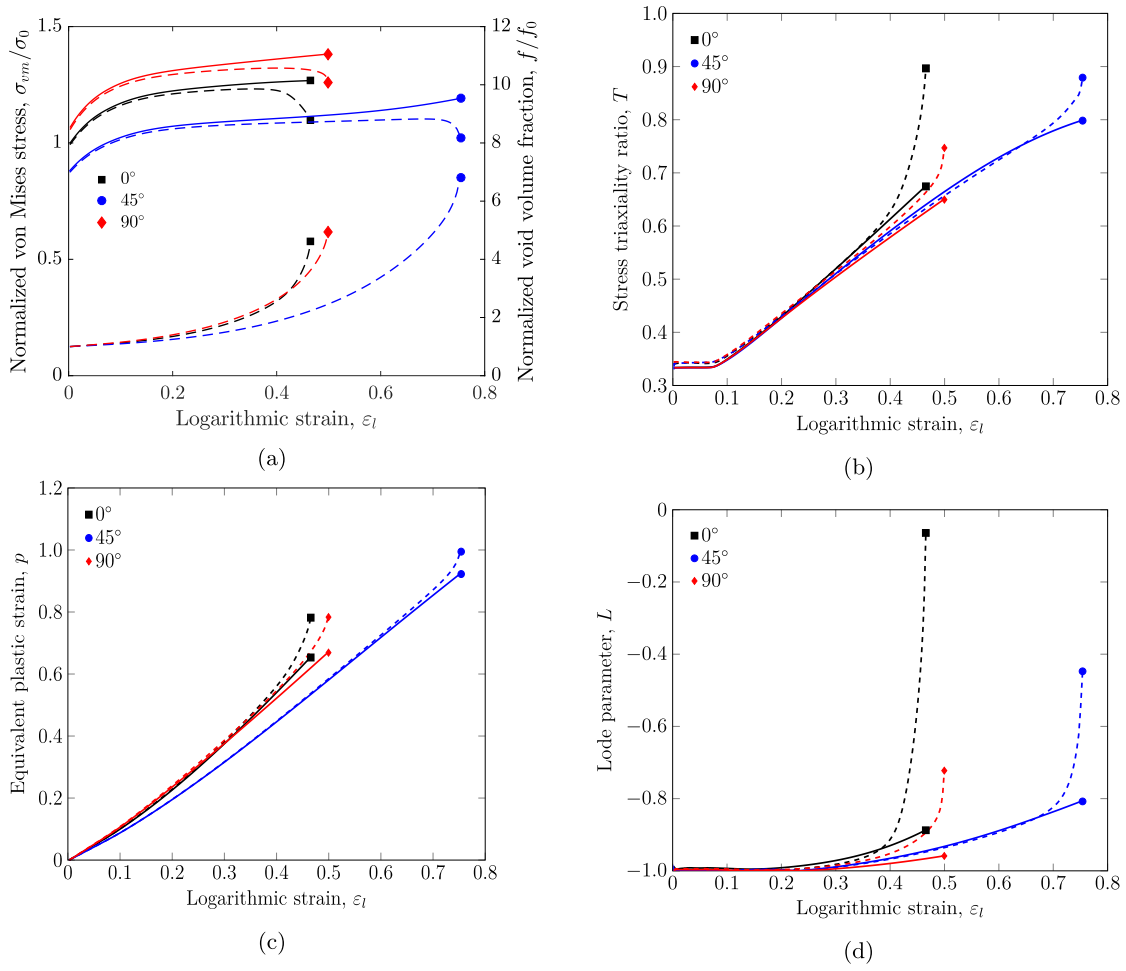

Fig. 14. Local behaviour in the regions inside (dashed lines) and outside (solid lines) of the imperfection band in the critical element for alloy B with temper T6 work hardening loaded in the ED-TD plane: (a) normalized von Mises stress and normalized void volume fraction, (b) stress triaxiality ratio, (c) equivalent plastic strain, and (d) Lode parameter versus logarithmic strain.

rameter evolve in a favourable way for localization, which is more important than the lower stress level.

6. Concluding remarks

Three aluminium alloys with different grain structure and crystallographic texture, solution heat-treated and artificially aged to three conditions giving different strength and work-hardening behaviours, were considered in the study. Previous experiments on these materials had shown that the tensile ductility of the alloys decreased with higher strength and lower work hardening, and the ductility was different depending on the alloy.

The influence of plastic anisotropy, strength and work hardening on ductile failure was studied by nonlinear finite element simulations and strain localization analyses of tensile tests in various directions. The anisotropic yield surfaces of the aluminium alloys, previously obtained by the crystal plasticity finite element method, were used to construct a set of model materials. These yield surfaces and an isotropic yield surface were combined with three flow stress curves representative for the different heat-treatments. Thus, a total of 12 model materials, with different plastic anisotropy, strength and work hardening were constructed and used in the numerical investigations. Finite element simulations of tensile tests on smooth axisymmetric specimens were conducted in seven in-plane directions, and the deformation gradient history extracted from the numerical simulations were used to drive the strain localization analyses.

Plastic anisotropy was found to have a marked influence on the tensile ductility and to induce failure anisotropy. The shape and extension of the regions of concentrated plastic flow in the finite element simulations varied with tensile direction for the anisotropic materials. The highly deformed regions were found to vary in shape so that the deformation mode at incipient ductile failure changes from a flat to a slant shear mode depending on the loading direction and plastic anisotropy. In agreement with experimental evidence from the literature (Fourmeau et al., 2013; Khadyko et al., 2019), the strain localization analyses predicted a variation of the failure strain with tensile direction that appears to correlate with the variation of the Lankford coefficient, thus indicating that the failure anisotropy is closely linked to the plastic anisotropy for these aluminium alloys.

The strain localization analyses predict a higher ductility for materials with lower strength and higher work hardening, as these features lead to a more uniform plastic strain distribution and a stress state with a lower stress triaxiality in the neck. The redistribution of plastic deformation due to the high work hardening makes the tensile specimen less prone to localization and ductile failure. The influence of strength and work hardening on the tensile ductility is also found to depend on the plastic anisotropy.

Acknowledgements

The financial support of this work from the Centre for Advanced Structural Analysis (CASA), Project No. 237885, Centre for

Please cite this article as: B.H. Frodal, D. Morin and T. Børvik et al., On the effect of plastic anisotropy, strength and work hardening on the tensile ductility of aluminium alloys, International Journal of Solids and Structures, https://doi.org/10.1016/j.ijsolstr.2019.10.003

Research-based Innovation (CRI) at the Norwegian University of Science and Technology (NTNU), is gratefully acknowledged.

References

Abaqus, 2014. Version 6.14. Dassault Systemès Simulia Corporation. Providence, Rhode Island, USA.
Agarwal, H., Gokhale, A.M., Graham, S., Horstemeyer, M.F., 2002. Anisotropy of intermetallic particle cracking damage evolution in an Al-Mg-Si base wrought aluminum alloy under uniaxial compression. Metallurgical and Materials Transactions A 33 (11), 3443–3448.
Barlat, F., Aretz, H., Yoon, J.W., Karabin, M.E., Brem, J.C., Dick, R.E., 2005. Linear transfomation-based anisotropic yield functions. Int. J. Plastic. 21 (5), 1009–1039.
Barsoum, I., Faleskog, J., 2007. Rupture mechanisms in combined tension and shear micromechanics. Int. J. Solid. Struct. 44 (17), 5481–5498.
Barsoum, I., Faleskog, J., 2011. Micromechanical analysis on the influence of the lode parameter on void growth and coalescence. Int. J. Solid. Struct. 48 (6), 925–938.
Benzerga, A.A., Besson, J., 2001. Plastic potentials for anisotropic porous solids. Eur. J. Mech.- A/Solid 20 (3), 397–434.
Benzerga, A.A., Thomas, N., Herrington, J.S., 2019. Plastic flow anisotropy drives shear fracture. Sci. Rep. 9 (1), 1425.
Chen, J., Madi, Y., Morgeneyer, T.F., Besson, J., 2011. Plastic flow and ductile rupture of a 2198 Al-Cu-Li aluminum alloy. Comput. Mater. Sci. 50 (4), 1365–1371.
Dunand, M., Mohr, D., 2014. Effect of lode parameter on plastic flow localization after proportional loading at low stress triaxialities. J. Mech. Phys. Solids 66, 133–153.
Dæhli, L.E.B., Børvik, T., Hopperstad, O.S., 2016. Influence of loading path on ductile fracture of tensile specimens made from aluminium alloys. Int. J. Solid Struct. 88, 17–34.
Dæhli, L.E.B., Faleskog, J., Børvik, T., Hopperstad, O.S., 2017. Unit cell simulations and porous plasticity modelling for strongly anisotropic FCC metals. Eur. J. Mech. - A/Solids 65, 360–383.
Dæhli, L.E.B., Hopperstad, O.S., Benallal, A., 2019. Effective behaviour of porous ductile solids with a non-quadratic isotropic matrix yield surface. J. Mech. Phys. Solid. 130, 56–81.
Dæhli, L.E.B., Morin, D., Børvik, T., Hopperstad, O.S., 2017. Influence of yield surface curvature on the macroscopic yielding and ductile failure of isotropic porous plastic materials. J. Mech. Phys. Solid 107, 253–283.
Engler, O., Randle, V., 2009. Introduction to Texture Analysis: Macrotexture, Microtexture, and Orientation Mapping, 2nd CRC press, Taylor & Francis Group.
Fourmeau, M., Børvik, T., Benallal, A., Hopperstad, O.S., 2013. Anisotropic failure modes of high-strength aluminium alloy under various stress states. Int. J. Plastic. 48, 34–53.
Fourmeau, M., Børvik, T., Benallal, A., Lademo, O.G., Hopperstad, O.S., 2011. On the plastic anisotropy of an aluminium alloy and its influence on constrained multiaxial flow. Int. J. Plastic. 27 (12), 2005–2025.
Frodal, B.H., Dæhli, L.E.B., Børvik, T., Hopperstad, O.S., 2019. Modelling and simulation of ductile failure in textured aluminium alloys subjected to compression-tension loading. Int. J. Plastic. 118, 36–69.
Frodal, B.H., Pedersen, K.O., Børvik, T., Hopperstad, O.S., 2017. Influence of pre-compression on the ductility of AA6xxx aluminium alloys. Int. J. Fract. 206 (2), 131–149.
Gruben, G., Morin, D., Langseth, M., Hopperstad, O.S., 2017. Strain localization and ductile fracture in advanced high-strength steel sheets. Eur. J. Mech. - A/Solids 61, 315–329.
Guo, T.F., Wong, W.H., 2018. Void-sheet analysis on macroscopic strain localization and void coalescence. J. Mech. Phys. Solid 118, 172–203.
Gurson, A.L., 1977. Continuum theory of ductile rupture by void nucleation and growth: part I yield criteria and flow rules for porous ductile media. J. Eng. Mater. Technol. 99 (1), 2–15.
Hannard, F., Pardoen, T., Maire, E., Bourlot, C.L., Mokso, R., Simar, A., 2016. Characterization and micromechanical modelling of microstructural heterogeneity effects on ductile fracture of 6xxx aluminium alloys. Acta Mater. 103, 558–572.
Hannard, F., Simar, A., Maire, E., Pardoen, T., 2018. Quantitative assessment of the impact of second phase particle arrangement on damage and fracture anisotropy. Acta Mater. 148, 456–466.
Keralavarma, S.M., Hoelscher, S., Benzerga, A.A., 2011. Void growth and coalescence in anisotropic plastic solids. Int. J. Solid. Struct. 48 (11), 1696–1710.
Khadyko, M., Dumoulin, S., Børvik, T., Hopperstad, O.S., 2014. An experimental-numerical method to determine the work-hardening of anisotropic ductile materials at large strains. Int. J. Mech. Sci. 88, 25–36.
Khadyko, M., Morin, D., Børvik, T., Hopperstad, O.S., 2019. Tensile ductility of extruded aluminium alloy AA6063 in different tempers. Mater. Sci. Eng. 744, 500–511.
Legarth, B.N., Tvergaard, V., 2018. Effects of plastic anisotropy and void shape on full three-dimensional void growth. J. Appl. Mech. 85 (5), 051007.
Lloyd, D.J., 2003. The scaling of the tensile ductile fracture strain with yield strength in al alloys. Scripta Mater. 48 (4), 341–344.
Marciniak, Z., Kuczyński, K., 1967. Limit strains in the processes of stretch-forming sheet metal. Int. J. Mech. Sci. 9 (9), 609–620.
Morin, D., Dæhli, L.E.B., Børvik, T., Benallal, A., Hopperstad, O.S., 2019. Numerical study of ductile failure under non-proportional loading. Eur. J. Mech. - A/Solids 74, 221–241.
Morin, D., Fourmeau, M., Børvik, T., Benallal, A., Hopperstad, O.S., 2018b. Anisotropic tensile failure of metals by the strain localization theory: an application to a high-strength aluminium alloy. Eur. J. Mech. - A/Solids 69, 99–112.
Morin, D., Hopperstad, O.S., Benallal, A., 2018a. On the description of ductile fracture in metals by the strain localization theory. Int. J. Fract. 209 (1), 27–51.
Nahshon, K., Hutchinson, J.W., 2008. Modification of the Gurson model for shear failure. Eur. J. Mech. - A/Solids 27 (1), 1–17.
Needleman, A., Rice, J.R., 1978. Limits to ductility set by plastic flow localization. Mech. Sheet Metal Form. 237–267.
Pedersen, K.O., Westermann, I., Furu, T., Børvik, T., Hopperstad, O.S., 2015. Influence of microstructure on work-hardening and ductile fracture of aluminium alloys. Mater. Des. 70, 31–44.
Pineau, A., Benzerga, A.A., Pardoen, T., 2016. Failure of metals I: brittle and ductile fracture. Acta Mater. 107, 424–483.
Reddi, D., Areej, V.K., Keralavarma, S.M., 2019. Ductile failure simulations using a multi-surface coupled damage-plasticity model. Int. J. Plastic. 118, 190–214.
Rice, J.R., 1976. Localization of plastic deformation. In: 14th International Congress of Theoretical and Applied Mechanics 207–220.
Rudnicki, J.W., Rice, J.R., 1975. Conditions for the localization of deformation in pressure-sensitive dilatant materials. J. Mech. Phys. Solid 23 (6), 371–394.
Steglich, D., Wafai, H., Besson, J., 2010. Interaction between anisotropic plastic deformation and damage evolution in al 2198 sheet metal. Eng. Fract. Mech. 77 (17), 3501–3518.
Tekoğlu, C., Hutchinson, J.W., Pardoen, T., 2015. On localization and void coalescence as a precursor to ductile fracture. Philos. Trans. R Soc. A 373 (2038), 20140121.
Tvergaard, V., 1981. Influence of voids on shear band instabilities under plane strain conditions. Int. J. Fract. 17 (4), 389–407.
Vishwakarma, V., Keralavarma, S.M., 2019. Micromechanical modeling and simulation of the loading path dependence of ductile failure by void growth to coalescence. Int. J. Solid Struct. 166, 135–153.
Westermann, I., Pedersen, K.O., Furu, T., Børvik, T., Hopperstad, O.S., 2014. Effects of particles and solutes on strength, work-hardening and ductile fracture of aluminium alloys. Mech. Mater. 79, 58–72.
Xue, Z., Faleskog, J., Hutchinson, J.W., 2013. Tension-torsion fracture experiments - Part II: simulations with the extended Gurson model and a ductile fracture criterion based on plastic strain. Int. J. Solid. Struct. 50 (25), 4258–4269.
Xue, Z., Pontin, M.G., Zok, F.W., Hutchinson, J.W., 2010. Calibration procedures for a computational model of ductile fracture. Eng. Fract. Mech. 77 (3), 492–509.
Zhang, H., Diehl, M., Roters, F., Raabe, D., 2016. A virtual laboratory using high resolution crystal plasticity simulations to determine the initial yield surface for sheet metal forming operations. Int. J. Plastic. 80, 111–138.
Zhang, K., Holmedal, B., Hopperstad, O.S., Dumoulin, S., Gawad, J., Van Bael, A., Van Houtte, P., 2015. Multi-level modelling of mechanical anisotropy of commercial pure aluminium plate: crystal plasticity models, advanced yield functions and parameter identification. Int. J. Plastic. 66, 3–30.

Please cite this article as: B.H. Frodal, D. Morin and T. Børvik et al., On the effect of plastic anisotropy, strength and work hardening on the tensile ductility of aluminium alloys, International Journal of Solids and Structures, https://doi.org/10.1016/j.ijsolstr.2019.10.003